CASL-U-2014-0139-000

Power uprates
and plant life extension

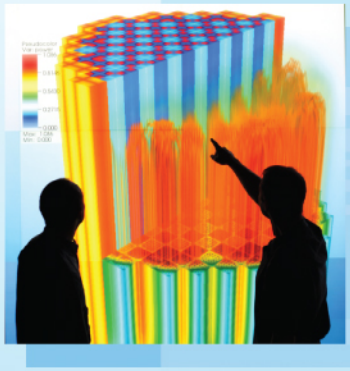

Engineering design
and analysis

Science-enabling
high performance
computing

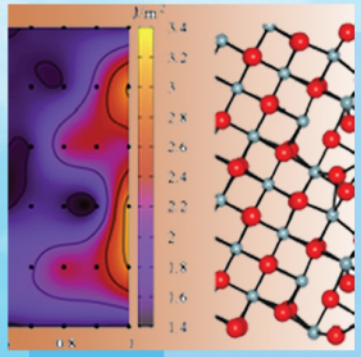

Fundamental science

Plant operational data

Consortium for Advanced Simulation of LWRs

Milestone L3:MPO.GTRF.P8.01

Microscale Model for Simulating Fretting Wear of Brittle Materials with Third-body Wear Debris Interaction

A. V. Hayrapetian and M. J. Demkowicz

Massachusetts Institute of Technology (MIT)

May 8, 2014

U.S. DEPARTMENT OF ENERGY | Nuclear Energy

Microscale model for simulating fretting wear of brittle materials with third-body wear debris interaction

A.V. Hayrapetian[a], M.J. Demkowicz[b,*]

[a]Department of Mechanical Engineering, Massachusetts Institute of Technology, Cambridge, MA 02139, USA
[b]Department of Materials Science and Engineering, Massachusetts Institute of Technology, Cambridge, MA 02139, USA

Abstract

Fretting wear models typically estimate wear rates using some form of a work-rate wear model with constant wear coefficients, but experimental results show that using a constant wear coefficient makes the wear model insufficient at modeling the complex dependence of the wear rate on various operating conditions of fretting wear. A new modeling framework is discussed that is designed with the goal of simulating abrasive/adhesive fretting wear mechanisms of brittle materials at the micron length-scale with the presence and interaction of third-body wear debris in order to study the effects of fretting operating conditions on wear rates. The capabilities of the model include the ability to generate new wear debris particles through brittle fracture of elastically-deforming asperities and modeling contact with friction and adhesion between any bodies in the simulation. These capabilities are demonstrated through two small simulations, and a validation study on the friction and sliding capabilities of the model is discussed through the simulation of a block sliding under gravity down an inclined plane.

Keywords: fretting wear, third body, wear debris, discrete element, contact

1. Introduction

Fretting wear is a common issue in many engineering applications. One particular application where it plays an important role is grid-to-rod fretting (GTRF) in nuclear reactors; GTRF is the cause of about 74% of leaking fuel incidents in light water-cooled nuclear fission reactors [1]. In GTRF, the turbulent coolant vibrates fuel rods against supporting grids which results in the wear of the thin cladding walls of the rod. Current attempts to model this process and estimate the rod lifetime, such as VITRAN (Vibration Transient Analysis Nonlinear) [2, 3], involve using work-rate wear models [4, 5] with constant empirical wear coefficients, in which the wear rate is considered to be proportional only to the rate of mechanical work done in the rubbing process. However, several experimental results have shown that a work-rate wear model with constant wear coefficients cannot properly model the complex dependency of the wear rate on various operating conditions.

In order to develop a better model to estimate wear rates under the variety of different possible operating conditions relevant in fretting wear, it is necessary to understand the mechanisms through which the changing operating conditions affect the rate of wear debris generation from the surface of the fretting materials. We have developed a modeling framework to dynamically simulate fretting wear mechanisms at the micron length-scale which can be used to study how wear debris is generated through colliding asperities on the surface of the two rough, brittle fretting materials, how accumulating third-body wear debris generated from wear play a role in the further evolution of the wear process, and how these processes vary with different operating conditions such as normal load, slip amplitude, material properties, type of fretting motion (pure sliding or a hybrid motion of sliding and impact), and other properties.

Currently, we have developed the framework and corresponding code for critical features for modeling wear of rough brittle materials, such as elasticity, contact, fracture, friction, and sliding. These capabilities are demonstrated through a simulation of two elastic circles pushed together in contact and sliding against each other with friction and also through a simulation of the fracture of a single asperity due to a collision with an obstacle. We have also partially validated the friction and sliding capabilities of the model through the case

*Corresponding author
Email addresses: areg@mit.edu (A.V. Hayrapetian), demkowicz@mit.edu (M.J. Demkowicz)

CASL-U-2014-0139-000

study of a block sliding down an inclined plane under gravity.

Many simulation techniques focused on modeling and understanding wear accurately model the forces, traction and slip between the geometries sliding against each other and then reduce the information from these simulations to a work rate to be used in a simple work-rate wear model with a constant wear coefficient. Typically the forces and slip calculations used to estimate the wear come from analytical expression from elastic solid mechanics [6, 7], or from finite element simulations [8, 9, 10]. In these simulations, progressive wearing of the surface is modeled, but wear debris is not included in the simulations. Attempts have been made to model the third-body wear debris in fretting wear simulations. The wear debris layer has been modeled as an anisotropic elastic-plastic material using finite elements in a fretting wear simulation using Archard's law in [11]; the model is capable enough to track the growth and shrinkage of the debris layer thickness through ejection of wear debris from the contact interface, but there are limitations in the model due to the requirement of using a continuum simplification of the discrete wear debris particles. A third-body layer of individual rigid debris particles modeled using discrete elements was used by [12] to study the effect of the third-body layer on the macroscopic friction behavior of two sliding bodies; however, the wear debris particles are included in the beginning of the simulation and cannot be generated through wear of surfaces.

Alternatives to fretting wear models based on work-rate in the literature appears to be limited to only modeling fatigue-based mechanisms of wear. These mechanisms have been studied in a 2-D numerical model [13] and in 3-D using the finite element method [14] to find the likely location of crack initiation and the number of cycles for initiation and propagation of the crack. An analytical model of fretting wear that is informed by finite element analysis but based solely on the fatigue-based mechanism of fretting wear has also been developed [15]. While these studies and models are useful for fatigue-based mechanisms, they do not address the challenge of modeling abrasive/adhesive wear mechanisms in a way that does not rely on the limited work-rate model.

Experiments by [16] and [17] of dry fretting wear between two metals show how a work-rate wear model with constant wear coefficients fail to predict the dependence of the wear rate on parameters such as normal load, slip amplitude of the oscillatory motion, and on the number of cycles. The results show that the wear coefficient in the work-rate model increases with slip amplitude rather than remaining constant. In particular, there is a large sudden increase in the wear coefficient at a particular slip amplitude which represents the transition from partial slip, during which fatigue-based mechanisms of wear like delamination [18] are dominant, to gross slip, in which the wear rate is accounted for mostly by abrasive and adhesive wear. The experimental results also show a decrease in the wear coefficient as the number of cycles increase, which can be explained by the increasing true area of contact between asperities (and thus decrease in local pressure) because asperities deform and surface roughness changes as the fretting process continues. These are just some of many experimental results that demonstrate the need to model wear rates through an understanding the micromechanical state of contact and not only a work-rate wear model with constant empirical wear coefficients. Other experiments [19, 20, 21, 22] show how the grid support geometry in the case of GTRF, further complicate wear rate predictions, and experiments on the dependence of the wear rate on a hybrid sliding/impact fretting motion by [23, 24] show that the wear coefficient can change by an order of magnitude simply by adjusting the type of fretting motion. These experimental results motivate our desire to understand how the wear coefficient varies with certain important operating conditions in fretting wear. And to do this, we plan to study the wear process using the modeling framework we developed which can simulate fretting wear mechanisms such as brittle abrasive wear of colliding asperities, interaction of third-body wear debris, and contact with adhesion and sliding friction of the fretting surfaces and wear debris.

2. Requirements for wear model

Experimental results have shown that a work-rate wear model with a constant wear coefficient is unable to model the complex dependence of the wear rate on operating conditions such as contact load, slip displacement, number of cycles, type of fretting motion, and more. By allowing the wear coefficient to not be constant but instead vary with these operating conditions, the work-rate wear model can become more useful for modeling fretting wear under more complicated scenarios. Understanding the dependence of the wear coefficient on the relevant operating conditions through experiments alone would require a huge combination of operating condition values which quickly become unfeasible. Instead, simulations providing the ability to study the mechanism through which changes in the operating conditions influence the wear process offer a tractable solution to creating a fretting wear mechanism

map and models of how the wear coefficient changes with operating conditions.

Different mechanisms of wear are already well known in the literature, such as ductile/brittle abrasive and adhesive wear, and fatigue-based mechanisms of wear. However, though fretting wear is often characterized by its tendency to collect wear debris in the contact region, a survey of the literature shows there has been limited analysis on the effect of the third-body layer on the wear rate. Experiments discussed in [25] showed that the third-body wear debris layer may reduce the wear rate by acting as a compacted lubricating layer or alternatively may increase the wear rate due to the abrasive behavior of the hard oxide debris particles; and, whether the wear debris is beneficial or harmful for wear depends on parameters such as the normal load and slip amplitude. Therefore, the main focus of our model is to understand the behavior of wear debris on wear rates and how changes in the operating conditions affect this behavior. For the model to be capable enough to allow for studying this behavior, we require a micron length-scale model, because that is the length scale of the wear debris, which can simulate the interaction and contact of individually tracked third-body wear debris particles with each other and with asperities on the surface of the two fretting materials, and which can also track the amount, size and shape of wear debris generated through the wearing process.

To simplify the requirements of the model while still remaining capable of handling our main focus, we restrict the model to brittle abrasive and adhesive wear through the brittle fracture of elastically deformed asperities. Ductility and plastic deformation can be safely ignored when modeling the wear of brittle materials, such as the zirconia oxide film that grows on the grid supports and fuel rod cladding in the case of GTRF. Also, abrasive and adhesive mechanism of wear dominate the influence on the wear rate compared to fatigue-based mechanisms of wear in the operating conditions of gross slip which is our primary regime of interest.

The strict requirements on the model to be incredibly flexible with regards to the possibility of contact between any surfaces in the simulations, including surfaces that are dynamically formed when new wear debris are generated, require a new method designed for this style of contact from the beginning. Inspiration for the model was taken from both molecular dynamics and more appropriately the discrete element method (DEM) in terms of the ability for discretely tracked elements in the system to interact with their neighbors which change as the simulation evolves. Unlike DEM, however, rigid particles could not be used because elastic strain is necessary to model the fracture of asperities and generate new wear debris. The elastic deformation of material simulated in the model is inspired by the finite element method, and in fact the model uses something similar to constant strain triangular finite elements in 2-D to model elasticity. Beyond contact, elastic deformation, and fracture, further requirements for the model include the need to properly model friction and adhesion between contacting surfaces. These requirements are satisfied in our model through modified dynamics of the contact mechanism. While it is ideal for the model to capable of working in 3-D, a 2-D model can still provide very useful results; our model is currently limited to 2-D as a simplification, although there is no foreseeable limitation in extending it to 3-D.

3. Methods

In this model, all elastic bodies are comprised of smaller bodies called discrete elements. Fig. 1 shows a typical discretization of two circular bodies into discrete elements. The discrete elements are not actually shown in that image because the discrete elements do not have a specified shape. The only state tracked for each discrete element e is its mass m_e, position $\mathbf{p}_e$, velocity $\mathbf{v}_e$, and effective size r_e. The discrete elements are represented by each of the vertices of the triangles in the figure. The discrete elements at the boundary of a body are called surface elements. Although all discrete elements have an effective size, in Fig. 1 the effective size of only the surface elements is visualized by the blue circles centered on the position of the elements; the radius of each circle in the visualization is set equal to the effective size of its corresponding element.

Neighboring discrete elements can join together to form a joint; the discrete elements forming the joint are called the members of the joint. Joints can be one of two types: interior joints or contact joints. Interior joints represent a solid connection between the joint's member elements; within an interior joint, there is contiguous matter bonded together that is shared between the member elements. Conversely, contact joints represent two independent solids that are merely in contact with one another. The space within a contact joint is divided into the two solids by a partition called the contact plane. In Fig. 1, both joints are visualized: the discrete elements in each of the two bodies are held together by interior joints, which are visualized in the figure by the green triangles (in 2-D) with black edges; also, the contact between the two bodies is represented through contact joints, which are visualized by the yellow triangles

CASL-U-2014-0139-000

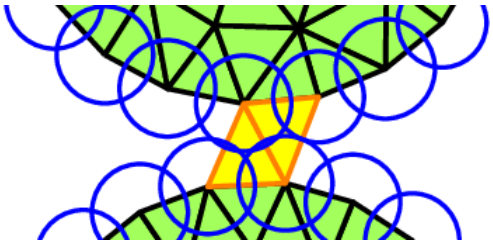

Fig. 1. Two circular bodies, which are each discretized by discrete elements held together with interior joints, are in a state of contact. The contact between the bodies is modeled using the contact joints.

with orange edges. All joints are able to model the elastic deformation of the material within the domain of the joint. Interior joints also provide the capability of fracture, and contact joints provide the capabilities of friction and adhesion.

3.1. Elasticity of joints

Elasticity is modeled within the joints. Both interior and contact joints can be deformed elastically, but the dynamics of contact joints are slightly more involved because the contact joints need to model the differences in the stress carrying capacity of contact joints, which is discussed in sections 3.3 and 3.4.

The displacement field $\mathbf{u}(\mathbf{X})$ of the matter within a joint is assumed to be fully described by a single deformation gradient tensor $\mathbf{F}$ for the joint such that the partial derivative of the displacement field with respect to material coordinates is $\frac{\partial \mathbf{u}}{\partial \mathbf{X}} = \mathbf{F} - \mathbf{I}$, where $\mathbf{I}$ is the identity tensor. Then, the displacement field within a joint can be determined if the reference configuration of the joint and the current positions of the joint's member elements are known. The reference configuration is the set of independent displacement vectors between the positions of the joint's member elements when the joint is in a stress-free state. For interior joints, the reference configuration is initially determined at the beginning of the simulation: it is either directly prescribed for each interior joint, or more likely it can be easily calculated from the initial positions of the elements if the interior joints at the start of the simulation are taken to be in a stress-free state.

In 2-D, exactly three discrete elements can form a joint, which has the shape of a triangle. The three member elements of joint j are e_1^j, e_2^j, and e_3^j, which are ordered such that the path drawn going from e_1^j to e_2^j to e_3^j and back to e_1^j turns in a counter-clockwise orientation. The vector $\mathbf{s}_i^j$ for $i \in \{1, 2, 3\}$ is the directed edge of the triangle associated with joint j that is opposite to the member element e_i^j. For example, $\mathbf{s}_1^j = \mathbf{p}_{e_3^j} - \mathbf{p}_{e_2^j}$ and $\mathbf{s}_2^j = \mathbf{p}_{e_1^j} - \mathbf{p}_{e_3^j}$. The reference configuration of joint j in 2-D is given by $\{\mathbf{w}_1^j, \mathbf{w}_2^j\}$. If a joint j is in the stress-free state at time $t = 0$, then the vectors of the reference configuration of joint j are given by $\mathbf{w}_1^j = \mathbf{s}_1^j(t = 0)$ and $\mathbf{w}_2^j = \mathbf{s}_2^j(t = 0)$, or some rotation of those vectors. If the current positions of the member elements of joint j at time t are known, and the reference configuration of joint j is also known, then the deformation gradient tensor $\mathbf{F}^j(t)$ that defines the displacement field within the joint j at time t can be calculated as follows:

$$\begin{aligned}\mathbf{F}^j(t) &= \begin{bmatrix}\mathbf{s}_1^j(t) & \mathbf{s}_2^j(t)\end{bmatrix}\begin{bmatrix}\mathbf{w}_1^j & \mathbf{w}_2^j\end{bmatrix}^{-1} \\ &= \begin{bmatrix}(\mathbf{p}_{e_3^j}(t) - \mathbf{p}_{e_2^j}(t)) & (\mathbf{p}_{e_1^j}(t) - \mathbf{p}_{e_3^j}(t))\end{bmatrix}\begin{bmatrix}\mathbf{w}_1^j & \mathbf{w}_2^j\end{bmatrix}^{-1}.\end{aligned} \tag{1}$$

While elasticity is modeled in the joints, the elastic response of a body under loads and deformation ultimately needs to come from the motion of the discrete elements that make up the body. The elements are just treated as point masses that move according to $\mathbf{f}_e = m_e \mathbf{a}_e = m_e \frac{\partial^2 \mathbf{p}_e}{\partial t^2}$. The net force on the element $\mathbf{f}_e$ needs to be selected to appropriately model a realistic elastic response. The net force is determined by conserving the energy of the system (sum of kinetic and potential energy). If the potential energy of the system is Π, then the net force on each element e is

$$\mathbf{f}_e = -\frac{\partial \Pi}{\partial \mathbf{p}_e}. \tag{2}$$

The potential energy of the elastic body with domain Ω and boundary Γ that has body forces $\mathbf{b}$ acting on the body and traction forces $\mathbf{t}$ acting on part of its boundary Γ_σ is given by

$$\Pi = \int_\Omega \mathcal{U} dA - \int_\Omega \mathbf{b} \cdot \mathbf{u} dA - \int_{\Gamma_\sigma} \mathbf{t} \cdot \mathbf{u} dS, \tag{3}$$

where $\mathcal{U}$ is the elastic strain energy density. Because the joints define where matter exists within a body and the joints do not overlap, the domain of a body Ω is the union of the disjoint domains of joints. If the domain of an joint j is Ω^j, then $\Omega = \bigcup_{\forall j} \Omega^j$ and

$$\Pi = \sum_{\forall j} \left[\int_{\Omega^j} \mathcal{U} dA - \int_{\Omega^j} \mathbf{b} \cdot \mathbf{u} dA \right], \tag{4}$$

assuming there are no tractions $\mathbf{t}$. Tractions are not typically useful for the wear simulations intended to be run

with this model. Tractions are not needed for contact because the contact joints directly model the contact, and prescribed tractions at the boundary of a body can be simulated by simply prescribing equivalent body forces on the surface elements of the body.

Combining (2) and (4) gives

$$\mathbf{f}_e = \sum_{\forall j} \left[-\int_{\Omega^j} \frac{\partial \mathcal{U}}{\partial \mathbf{p}_e} dA + \int_{\Omega^j} \frac{\partial (\mathbf{b} \cdot \mathbf{u})}{\partial \mathbf{p}_e} dA \right]. \tag{5}$$

$\mathcal{J}_e$ is defined as the set of joints that the discrete element e belongs to as a member. By recognizing that the strain energy density $\mathcal{U}(\mathbf{x})$, body force $\mathbf{b}(\mathbf{x})$, and displacement $\mathbf{u}(\mathbf{x})$ only depend on $\mathbf{p}_e$ when $\mathbf{x} \in \bigcup_{j \in \mathcal{J}_e} \Omega^j$, (5) can be written as

$$\begin{aligned} \mathbf{f}_e &= \mathbf{f}_e^{\text{elastic}} + \mathbf{f}_e^{\text{body}} \\ &= -\sum_{j \in \mathcal{J}_e} \int_{\Omega^j} \frac{\partial \mathcal{U}}{\partial \mathbf{p}_e} dA + \sum_{j \in \mathcal{J}_e} \int_{\Omega^j} \frac{\partial (\mathbf{b} \cdot \mathbf{u})}{\partial \mathbf{p}_e} dA, \end{aligned} \tag{6}$$

where

$$\mathbf{f}_e^{\text{elastic}} = -\sum_{j \in \mathcal{J}_e} \int_{\Omega^j} \frac{\partial \mathcal{U}}{\partial \mathbf{p}_e} dA, \tag{7}$$

and

$$\mathbf{f}_e^{\text{body}} = \sum_{j \in \mathcal{J}_e} \int_{\Omega^j} \frac{\partial (\mathbf{b} \cdot \mathbf{u})}{\partial \mathbf{p}_e} dA. \tag{8}$$

Under the approximating assumption that the body force $\mathbf{b}(\mathbf{x})$ is homogeneous over the domain of a single joint j, or $\mathbf{b}(\mathbf{x}) = \mathbf{b}^j$ for $\mathbf{x} \in \Omega^j$, the contribution to the net force due to body forces, equation (8), reduces in the 2-D model to

$$\mathbf{f}_e^{\text{body}} = \frac{1}{3} \sum_{j \in \mathcal{J}_e} A^j \mathbf{b}^j, \tag{9}$$

where A^j is the area of the joint j. Usually the body force is due to an acceleration, such as the acceleration due to gravity $\mathbf{g}$. In that case, the body force is $\mathbf{b} = \rho \mathbf{g}$, where ρ is the density of the material, which is assumed to be homogeneous over the domain of a single joint. Applying gravity as a body force can be greatly simplified by selecting appropriate masses for the discrete elements. By selecting the mass of the elements at the start of the simulation according to

$$m_e = \frac{1}{3} \sum_{j \in \mathcal{J}_e} \rho^j A^j, \tag{10}$$

where ρ^j is the homogeneous density of the material within the joint j, (9) is further simplified to $\mathbf{f}_e^{\text{body}} = m_e \mathbf{g}$ for the case of the body force being due to an acceleration $\mathbf{g}$.

The general form of the potential energy in (3) allows for any hyperelastic material to be used in the model. However, to actually calculate $\mathbf{f}_e^{\text{elastic}}$ in (7), a specific material model must be chosen to get an expression for the strain energy density. The Saint Venant-Kirchoff material [26] was chosen for the current implementation of the model, which is an isotropic material with strain energy density

$$\mathcal{U} = \frac{1}{2} \lambda (\operatorname{tr} \mathbf{E})^2 + \mu \operatorname{tr}(\mathbf{E}^2), \tag{11}$$

where λ and μ are the Lamé constants, and $\mathbf{E}$ is the Lagrangian Green strain given by

$$\mathbf{E} = \frac{1}{2} (\mathbf{F}^\intercal \mathbf{F} - \mathbf{I}). \tag{12}$$

With the selection of the Saint Venant-Kirchoff material model, the contribution to the net force due to elasticity, equation (7), reduces in 2-D model to

$$\mathbf{f}_e^{\text{elastic}} = \sum_{j \in \mathcal{J}_e} \left[\frac{1}{2} \boldsymbol{\sigma}^j \mathbf{R}_{\frac{\pi}{2}} \mathbf{s}^j_{M_e^j} \right]. \tag{13}$$

$M_e^j \in \{1, 2, 3\}$ is an index map such that $M^j_{e_i^j} = i \ \forall i \in \{1, 2, 3\}$. $\mathbf{R}_{\frac{\pi}{2}}$ is a rotation matrix that rotates vectors counter-clockwise by 90° and is defined by

$$R_{\frac{\pi}{2}} = \begin{bmatrix} 0 & -1 \\ 1 & 0 \end{bmatrix}.$$

$\boldsymbol{\sigma}^j$ is the Cauchy stress in the joint j and is given by

$$\boldsymbol{\sigma}^j = \frac{1}{\det \mathbf{F}^j} \mathbf{F}^j \mathbf{S}^j (\mathbf{F}^j)^\intercal, \tag{14}$$

where $\mathbf{S}^j$ is the second Piola-Kirchoff stress in joint j and relates to the Lagrangian Green strain $\mathbf{E}^j = \frac{1}{2}((\mathbf{F}^j)^\intercal \mathbf{F}^j - \mathbf{I})$ in the joint j according to

$$\mathbf{S}^j = \lambda (\operatorname{tr} \mathbf{E}^j) \mathbf{I} + 2\mu \mathbf{E}^j. \tag{15}$$

3.2. Fracture of interior joints

Fracture is modeled by simply removing interior joints when a fracture condition has been met for the interior joint. Because the mass and velocity is tracked with the discrete elements and not the joints, mass and linear/angular momentum is conserved in the fracture process.

In general, the fracture condition can come from a cohesive zone model. In the current implementation of the

model, a very simple fracture algorithm is used in which the interior joint is removed if the maximum principal Cauchy stress in the interior joint exceeds some threshold value σ_{ft}.

To roughly estimate that threshold value the fracture toughness K_{Ic} and linear elastic fracture mechanics are used. Assuming a symmetric crack of width $2a$ oriented in the worse possible direction, and assuming the crack can be approximately modeled as existing in an infinite body with a far field stress σ^{∞}, the stress intensity factor from linear elastic fracture mechanics is $K_{\mathrm{I}} = \sigma^{\infty}\sqrt{\pi a}$. Fracture occurs when $K_{\mathrm{I}} = K_{\mathrm{Ic}}$, so $K_{\mathrm{Ic}} = \sigma_{ft}\sqrt{\pi a}$. Therefore, the fracture threshold is estimated as

$$\sigma_{ft} = \frac{K_{\mathrm{Ic}}}{\sqrt{\pi a}}, \tag{16}$$

where a is taken to be some fraction of the length scale of the interior joint.

When an interior joint is fractured, the member elements of the joint become surface elements. Because of this, they can later join together into contact joints to model contact. Discrete elements from a freshly fractured interior joint can immediately come together to form a stress-free contact joint, in which case, the model is simulating the process of the material fracturing but not actually separating from each other by a significant distance. The material can then later separate as the discrete elements are pulled apart, eventually causing the contact joint to be removed. The details of this processare discussed in section 3.3.2.

3.3. Contact joints

There are some important differences between contact joints and interior joints. While the matter within the domain of an interior joint is supposed to be bonded together as part of a solid body, the matter in contact joints consists of two independent solids that are just in contact with one another. The domain of the contact joint is divided by a partition called the contact plane. In 2-D, this contact plane is actually just a line, and it is always parallel to the edge from the joint's member elements e_1^j to e_2^j and located in between the edge and the third member element e_3^j. Within the domain of the contact joint, the matter on one side of the contact plane belongs to one body while the matter on the other side of the contact plane belongs to another body. It may be possible that the two solids are actually parts of a larger single body, but at the scale of an individual contact joint, they appear to be from different bodies. Since within the domain of the contact joint, there are two bodies that are in contact, the ability to transfer tension and shear between the two bodies is limited. In particular, a tensile load above some adhesive threshold will cause the two bodies to separate, thus removing the contact joint, and a shear load above a frictional limit will cause bodies to slip along the contact plane, thus severely deforming the contact joint. Severe deformation due to slipping can also cause the bodies to slide off one another which also leads to the removal of the contact joint. Finally, the contact joints need to be created in the first place to represent contact between two bodies that were originally not in contact and prevent them from passing through each other. All of these differences between contact joints and interior joints are discussed in detail in the remainder of section 3.

3.3.1. Forming contact joints

There are restrictions on how contact joints can be formed. First, only surface element can join together to form a contact joint. In particular, the first two surface elements of a contact joint, e_1^j and e_2^j, need to be belong to a directed edge from e_2^j to e_1^j that is a boundary edge. A boundary edge is any directed edge between surface elements that belongs to any interior joint. Second, a contact joint cannot be created that uses a directed edge that already exists (an edge between identical discrete elements but in the opposite direction is fine). These two constraints prevent contact joints from forming that could overlap with each other or an interior joint. Finally, the most important constraint on forming contact joints is the proximity constraint which only allows surface discrete elements to form a contact joint if they are "close enough" to one another.

The proximity constraint determines when the surface of two bodies are close enough to be considered in contact. The actual surface of a body discretized with discrete elements is not tracked in this model because the discrete elements making up the body do not have a defined shape. Instead the surface of a body can be approximated by the location of the surface elements and each of their effective sizes. For example, in Fig. 1, although the black edges of the triangles near the surface in each of the bodies are far apart from one another, the two bodies in that figure are actually touching (although just barely). The extent of the blue circles, which represent the effective size of the discrete elements, gives a vague approximation of the actual surface of the bodies. The condition used in the current model to determine whether the proximity constraint is satisfied for a candidate contact joint j is to check if both e_1^j is close enough to e_3^j and if e_2^j is close enough to e_3^j. Checking whether e_1^j is close enough to e_2^j is unnecessary because they must be part of a boundary edge and are therefore

always assumed to be close enough. For two elements to be considered "close enough" to one another, we require the distance between the two elements to be less than the sum of their effective sizes. Therefore, the proximity constraint of a candidate contact joint j is satisfied if $\|\mathbf{p}_{e_3^j} - \mathbf{p}_{e_1^j}\| < r_{e_3^j} + r_{e_1^j}$ and $\|\mathbf{p}_{e_3^j} - \mathbf{p}_{e_2^j}\| < r_{e_3^j} + r_{e_2^j}$.

The effective size of each of the elements is determined before the start of the simulation. It is desirable to choose an effective size such that circles centered on the elements with radii set to the effective size of the elements would have some overlap with adjacent circles, but at the same time not be too big. Each joint has some characteristic length which in 2-D is defined as the square root of the area of the joint. Choosing the effective size of an element through a weighted average of the characteristic lengths of the joints that the element belongs to as a member, where the weights are determined from the areas of the joints, was found to provide the best results. Mathematically, the effective size of an element e is

$$r_e = c \sum_{j \in \mathcal{J}_e} a_e^j \sqrt{A^j}, \tag{17}$$

where the weights a_e^j are given by

$$a_e^j = \frac{A^j}{\left(\sum_{\tilde{j} \in \mathcal{J}_e} A^{\tilde{j}}\right)}, \tag{18}$$

and c is a constant to universally adjust the weights. A constant of $c = 0.9$ was used to provide good results.

If the constraints for forming a contact joint are all satisfied, the contact joint must be created. Currently the implementation of the model iterates though the pairs of elements of all boundary edges and for each pair iterates through all surface elements in the simulation looking for a third element that can form a contact joint that satisfy all the constraints. If there are more than one valid candidates for the third element, the element closest to the boundary edge is chosen. The computational complexity of this naive algorithm is of order N^2, where N is the number of surface elements at any given time in the simulation, but restricting the search space to only nearby surface elements by using data structures like quadtrees can reduce the computational complexity of the algorithm to be linear with N.

3.3.2. Breaking contact joints

Contact joints must be removed when the joints member elements should no longer be considered to be in contact. This can happen if the surfaces are pulled apart from one another, but it can also happen if one surface slides away from another surface. In reality, if there is any amount of slipping that occurs at a point, the two material points that were originally coincident prior to slipping will no longer be in contact after slipping occurs. In the model, this is approximated by considering the two surfaces represented by a contact joint to be in contact even with some amount of sliding (which is discussed in section 3.4) until the sliding becomes too great that the surfaces cannot reasonably be considered in contact anymore. These two different ways of ending contact are modeled by removing the contact joints if either of two conditions are satisfied: the pull apart condition or the slide off condition.

The slide off condition is satisfied for contact joint j if the projection of e_3^j onto the boundary edge from e_1^j to e_2^j is far away from the boundary edge. Mathematically, this means the slide off condition is satisfied if either $(\mathbf{s}_1^j \cdot \mathbf{s}_3^j)/\|\mathbf{s}_3^j\|^2$ or $(\mathbf{s}_2^j \cdot \mathbf{s}_3^j)/\|\mathbf{s}_3^j\|^2$ is greater than some positive threshold value. We have currently selected a threshold of 0.50, which represents the slide off condition being met if the projection of e_3^j extends beyond the nearest vertex of the boundary edge by an amount greater than 50% of the length of the boundary edge.

The pull apart condition is determined from the stress state in the contact joint. In a non-adhesive contact, the contact joint could not take any tensile load normal to the contact plane. We extend this concept in order to provide a very simple model of adhesion by considering the contact to be pulled apart only if the normal tensile stress σ_n exceeds some threshold value σ_{at}. So, the pull apart condition is satisfied if $\sigma_n > \sigma_{at}$. The pull apart condition can be updated in the future with more sophisticated models of adhesion.

3.4. Friction

In this model, friction is modeled through the evolution of the reference configuration of contact joints. With a given reference configuration, the stress state in a contact joint changes as the current configuration evolves due to the moving member discrete elements. The stress state can be used to determine the tangential load T and normal load N acting on the slip plane of the contact joint. So, in general the tangential and normal loads of contact joint j are functions of the reference and current configurations: $T^j = \hat{T}(\mathbf{s}_1^j, \mathbf{s}_2^j, \mathbf{w}_1^j, \mathbf{w}_2^j)$ and $N^j = \hat{N}(\mathbf{s}_1^j, \mathbf{s}_2^j, \mathbf{w}_1^j, \mathbf{w}_2^j)$, where the non-linear functions $\hat{T}$ and $\hat{N}$ are known and depend on the elastic properties of the material within a contact joint which does not change throughout the lifetime of that contact joint.

To model friction, restrictions are placed on the tangential force. The contact joints cannot carry a tangen-

tial force that is greater in magnitude than the friction limit $\mu|N|$, where the coefficient of friction μ is the coefficient of static friction μ_s under the conditions of stick or is the coefficient of kinetic friction μ_k under the conditions of slip.

During each iteration in a simulation, the discrete element positions are updated and the deformation and stress state within each joint is calculated. During the updating stage, each contact joint j must satisfy the restriction on the tangential force described above: $|T^j(t_n)| \leq \mu|N^j(t_n)|$. To satisfy this requirement, the reference state is adjusted in a constrained manner to simulate the slipping phenomena. In 2-D, the contact plane is an line, so a unit vector $\hat{\mathbf{t}}^j$ parallel to that line representing the contact plane of contact joint j is used; the vector $\hat{\mathbf{t}}^j$ is actually defined in the reference space so that it is parallel to the vector $-(\mathbf{w}_1^j + \mathbf{w}_2^j)$. After the discrete element positions have been updated, the vectors $\mathbf{s}_1^j(t_n)$ and $\mathbf{s}_2^j(t_n)$ are known. The reference configuration of the contact joint in the prior iteration, $\{\mathbf{w}_1^j(t_{n-1}), \mathbf{w}_2^j(t_{n-1})\}$, is also known. If $|\hat{T}(\mathbf{s}_1^j(t_n), \mathbf{s}_2^j(t_n), \mathbf{w}_1^j(t_{n-1}), \mathbf{w}_2^j(t_{n-1}))| \leq \mu|\hat{N}(\mathbf{s}_1^j(t_n), \mathbf{s}_2^j(t_n), \mathbf{w}_1^j(t_{n-1}), \mathbf{w}_2^j(t_{n-1}))|$, then the condition is satisfied with the current reference configuration, and thus $\mathbf{w}_1^j(t_n) = \mathbf{w}_1^j(t_{n-1})$ and $\mathbf{w}_2^j(t_n) = \mathbf{w}_2^j(t_{n-1})$. On the other hand, if that inequality is not satisfied, then the following non-linear equation,

$$|\hat{T}(\mathbf{s}_1^j(t_n), \mathbf{s}_2^j(t_n), \mathbf{w}_1^j(t_{n-1}) + s_n^j\hat{\mathbf{t}}^j, \mathbf{w}_2^j(t_{n-1}) + s_n^j\hat{\mathbf{t}}^j)| = \mu|\hat{N}(\mathbf{s}_1^j(t_n), \mathbf{s}_2^j(t_n), \mathbf{w}_1^j(t_{n-1}) + s_n^j\hat{\mathbf{t}}^j, \mathbf{w}_2^j(t_{n-1}) + s_n^j\hat{\mathbf{t}}^j)|, \tag{19}$$

needs to be solved for the single degree of freedom s_n^j, which is the amount of slipping that occurs in contact joint j from time t_{n-1} to t_n. After solving for s_n^j, the new reference configuration for the contact joint j is given by:

$$\mathbf{w}_1^j(t_n) = \mathbf{w}_1^j(t_{n-1}) + s_n^j\hat{\mathbf{t}}^j,$$

and

$$\mathbf{w}_2^j(t_n) = \mathbf{w}_2^j(t_{n-1}) + s_n^j\hat{\mathbf{t}}^j.$$

3.5. Remeshing of contact joints

3.5.1. Reason for remeshing

Fig. 2 shows a sequence of steps in a simulation of two surfaces in sliding contact. The domain of each of the joints visualized in the figure are uniquely colored to aid in understanding what is occurring during these steps. Also, the edges of the interior joints are colored black, while the edges of the contact joints are colored orange. As the sliding progresses, the contact joints are deforming under shear considerably because they are undergoing slip. If the joints were to continue to deform, eventually the slide off condition discussed in section 3.3.2 would be satisfied and the contact joints would be removed. It is not ideal for contact joints to be removed and recreated from one time step to another in the simulations when in reality there is always a smooth gradual change in the contact conditions; the stress state of the newly formed contact joints would not carry over the elastic shear deformation and normal loading of the preceding contact joints, and thus the total normal and tangential loads would periodically fluctuate with discontinuous jumps in the loads instead of remaining stable. To overcome these issues, the concept of remeshing adjacent contact joints is introduced.

An example of the remeshing process can be seen in Fig. 2 in the transition from step 2 to step 3. The yellow and orange contact joints in step 2 are replaced with two new contact joints of a slightly different, desaturated, yellow and orange color. Similarly, the dark green and blue contact joints in step 2 are replaced in step 3 with the light green and light blue contact joints. The changes from step 2 to step 3 does not simply consist of removing the old contact joints and forming new ones according to the procedures in sections 3.3.1 and 3.3.2. Instead, the adjacent contact joints are instantaneously replaced within a single time step and the reference configuration of the new contact joints is carefully selected to maintain certain invariants which is discussed in section 3.5.3.

Fig. 2 also demonstrates how the remeshing procedure allows for long-distance sliding. The quadrilateral formed by the desaturated orange contact joint and light blue contact joint in step 4, is roughly the same shape as the quadrilateral formed by the dark green contact joint and dark blue contact joint in step 1. The two quadrilaterals also involve the same surface elements of the bottom surface. However, the surface elements of the orange-blue quadrilateral of step 4 involves a different pair of top surface elements than the pair of top surface elements taking part in the green-blue quadrilateral of step 1. In fact, the top surface elements involved have been shifted over by one element to the left along the boundary edge due to the fact that the top surface is sliding towards the right. This process could continue, leading to discrete elements in contact several steps later that were originally a very large distance apart. And while the long-distance sliding takes place, the contact joints could be continuously updated through remeshing so that at any given time there is always stable contact (represented through the contact joints) between the two bodies.

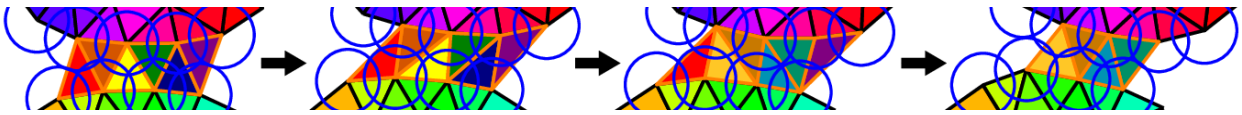

Fig. 2. Two surfaces in sliding contact causing the contact joints to be remeshed.

3.5.2. Remeshing conditions

Remeshing of skewed adjacent contact joints needs to occur before the slide off condition has been satisfied causing the contact joints to be removed. Of course sometimes, it is desirable to allow the slide off condition to be satisfied for a contact joint. For example, in Fig. 2, the red contact joint is adjacent to the yellow contact joint in step 3. Then, from step 3 to step 4, the red contact joint is removed due to the slide off mechanism. In this case, this is desired behavior and it would not be desirable to attempt remeshing the red and yellow contact joints. Another example of when remeshing would be undesirable is in step 1 of Fig. 2. The orange and yellow contact joints will eventually be remeshed right after step 2, but it is not desirable to prematurely remesh the orange and yellow contact joints in step 1 because they would become even more skewed than they already. The desired behavior for remeshing can be achieved by only remeshing if two conditions are satisfied.

The first condition is a check to make sure that remeshing would not create contact joints that overlap. For example, if an attempt was made to remesh the red and yellow contact joints in step 3 of Fig. 2, the resulting new contact joints would actually overlap with each other and with some of the interior joints of the bottom body. This is clearly unacceptable, so this potential problem is avoided by verifying that none of the interior angles of the quadrilateral formed by the adjacent contact joints have an angle greater than 180°.

The second condition that must be satisfied is called the skewness condition, which requires that the shape of the new contact joints after remeshing be less skewed than the shape of the contact joints before remeshing. More precisely, the skewness of a contact joint is measured by a metric called the shape factor. For a 2-D contact joint, the shape factor is the minimum of the cosines of the angles of the contact joint. Less skewed contact joints have larger shape factors. The shape factor has a maximum value of 0.5 for the least skewed contact joint, which has the shape of an equilateral triangle. So, if adjacent joints j_1 and j_2 are being considered for remeshing into new adjacent contact joints j_3 and j_4, the skewness condition is satisfied if $\mathrm{SF}_{j_1} + \mathrm{SF}_{j_2} < \mathrm{SF}_{j_3} + \mathrm{SF}_{j_4}$, where SF_j is the shape factor of contact joint j.

3.5.3. Invariants

When it is appropriate to remesh adjacent contact joints, the new contact joints that replace the previous ones each require a reference configuration. The reference configurations are selected to maintain certain invariants that must hold throughout the remeshing process. These invariants come from the conservation of linear/angular momentum and the conservation of energy; the conservation of mass is automatically satisfied because the discrete elements are not created or destroyed.

Remeshing can be better understood by considering the example of remeshing adjacent contact joints j_1 and j_2 into new contact joints j_3 and j_4. Contact joints j_1 and j_2 form a quadrilateral in 2-D with elements e_1, e_2, e_3, and e_4 at the vertices of the quadrilateral. The path from e_1 to e_2 to e_3 to e_4 and back to e_1 turns in a counterclockwise orientation. The edge vectors of the quadrilateral are known and can be calculated from the known vectors $\mathbf{s}_1^{j_1}$, $\mathbf{s}_2^{j_1}$, $\mathbf{s}_1^{j_2}$, $\mathbf{s}_2^{j_2}$. The four forces acting on the elements of the quadrilateral due to the elastic contributions of contact joints j_1 and j_2 only are also known from (13). For linear momentum to be conserved, the net force on each element after remeshing should remain the same as it was prior to remeshing. This means that the four forces acting on the elements of the quadrilateral due to elastic contributions of only contact joints j_3 and j_4 should be the same as the four forces acting on the elements due to elastic contributions of only contact joints j_1 and j_2. This imposes 8 constraints (four 2-D forces) on the reference configuration vectors $\mathbf{w}_1^{j_3}$, $\mathbf{w}_2^{j_3}$, $\mathbf{w}_1^{j_4}$, and $\mathbf{w}_2^{j_4}$ because the edges of joints j_3 and j_4 ($\mathbf{s}_1^{j_3}$, $\mathbf{s}_2^{j_3}$, $\mathbf{s}_1^{j_4}$, $\mathbf{s}_2^{j_4}$) are fixed to satisfy the known edge vectors of the quadrilateral. Two of those 8 constraints are redundant due to the conservation of linear momentum and one additional constraint is redundant due to the conservation of angular momentum. So, the forces on the elements of the quadrilateral impose only 5 constraints on the reference configuration vectors that need to be solved. The reference configuration vectors have a total of 6 degrees of freedom in 2-D (one of the four reference configuration vectors is redundant because two of the four reference configuration vectors will always be equal and opposite). The additional constraint needed

to solve the problem comes from the conservation of energy. The elastic strain energy in the quadrilateral prior to remeshing must equal the elastic strain energy in the quadrilateral after remeshing, or $U^{j_1} + U^{j_2} = U^{j_3} + U^{j_4}$, where U^j is the strain energy of joint j.

So, satisfying the invariants during the remeshing procedure requires solving a system of six non-linear equations for six unknowns. The unknowns are the independent variables defining the referencing configurations of the two new contact joints j_3 and j_4. Five of the six equations satisfy conservation of momentum, and the sixth equation satisfies conservation of energy. The equations are non-linear because of the non-linear dependence of the forces and strain energy density to the reference configuration, as can be seen through equations (1), (11), (12), (13), (14), and (15).

3.6. Time integration scheme and boundary conditions

With the forces on the elements known from (6), (9), and (13), the positions of the elements $\mathbf{p}_e(t)$ can be evolved using explicit time integration according to Newton's equation of motion $\mathbf{f}_e = m_e \frac{\partial^2 \mathbf{p}_e}{\partial t^2}$. The current implementation of the model uses an explicit linear multistep method for the time integration, in particular the fourth-order Adams–Bashforth method.

As mentioned before, traction boundary conditions are simulated by assigning an appropriate body force to the surface discrete elements that are part of the boundary that the traction would be applied to. For example, a uniform traction of $\mathbf{t}$ applied to an edge of length L connecting elements e_1 and e_2 is satisfied by applying a body force of $\frac{1}{2}L\mathbf{t}$ to each of the elements e_1 and e_2.

Displacement boundary conditions are easy to control because the simulation tracks the positions of the discrete elements. The simulation allows for various types of displacement boundary conditions. Some of the discrete elements can be selected to be restrained in their motion in some way. For example, a roller support can be simulated by preventing a change in the position of an element in one direction while allowing for movement in the perpendicular direction. This boundary condition is simulated in simulations by modifying the velocity vector to be consistent with the boundary condition. Another way the simulation allows handling displacement boundary conditions is by directly controlling the position of some discrete elements over time. This boundary condition is simulated by modifying the current configuration of discrete elements at each time step to be consistent with the imposed displacements.

4. Applications/Validation

The capabilities of this model, such as elasticity, fracture, contact, friction, adhesion, long-distance sliding, and tracking third-bodies, are demonstrated with two simple simulations. The first simulation consists of two elastic circles coming into contact and sliding against each other to demonstrate the capabilities of contact, friction, and long distance-sliding through the use of remeshing. The second simulation demonstrates a typical wear mechanism: an asperity coming into contact and breaking off due to fracture from the elastic straining in the asperity and becoming a new wear debris particle that is properly tracked in the simulation. Then, the case of a block sliding down an inclined plane is studied to act as a partial validation on some of the capabilities of the model. For all of these simulations, the material parameters (which are typical values for zirconia oxide) are: Young's modulus $E = 200\,\mathrm{GPa}$, Poisson's ratio $\nu = 0.3$, fracture toughness $K_{\mathrm{Ic}} = 13\,\mathrm{MPa\,m^{1/2}}$, and density $\rho = 6\,\mathrm{g\,cm^{-3}}$.

In the visualizations of the simulations that are shown in the figures, the discrete elements themselves, which are located at the vertices of the triangles representing the joints, are not shown. However, only for discrete elements at the surface, the effective sizes of the elements are shown with blue circles centered at the location of the elements. Triangles with black edges represent the interior joints, and triangles with orange edges represent the contact joints. The contact joints have a preferred orientation that defines the contact plane, but the contact planes are not shown in the visualizations below. The σ_{yy} component of the Cauchy stress within each joint (both interior and contact) are visualized through color plots.

4.1. Circles in contact

In the first simulation, two circular bodies are brought into contact with each other by holding the bottom half of the bottom body fixed and driving the top half of the top body downward until a compressive contact is formed between the two elastic circular bodies, shown in Fig. 3a. The orange-bordered contact joint in that figure show the state of elastic contact between the two bodies. The number of contact joints increase as the compression grows, which demonstrate the increasing area of contact between the two elastic circles in contact.

The top half of the top circular body is then moved rigidly to the right to allow the circles to slide against each other with friction. Fig. 3b show how the contact joints have deformed under shear to represent sliding

CASL-U-2014-0139-000

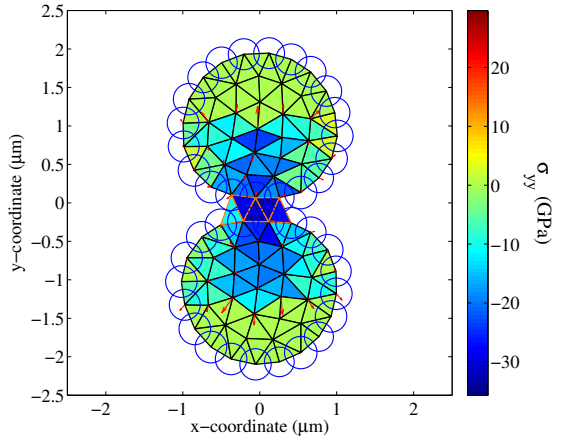

(a) Snapshot at t = 1.488 ns

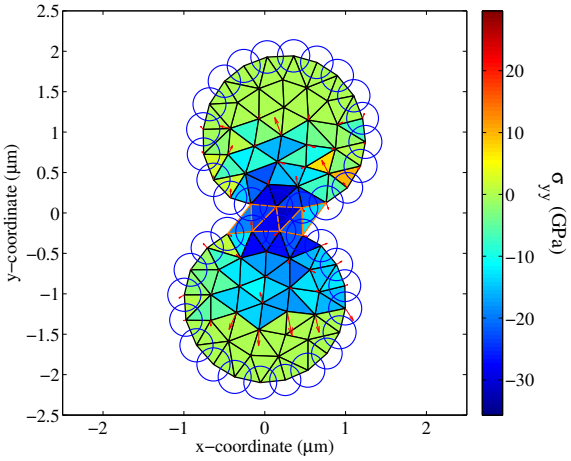

(b) Snapshot at t = 3.537 ns

Fig. 3. Snapshots of the simulation of circles in contact.

under friction. Some of the shear is carried elastically by the contact joint until a limit, after which point the further deformation of the triangle is due to slipping. A little later in the simulation, see Fig. 3c, the deformation of the contact joints has become so severe that an automatic remesh occurred to allow for further sliding.

As sliding continues, the contact joints move along the surface of the circular body but because the two bodies are getting further apart with additional sliding, the compressive loading in the contact joints is reduced, as seen in Fig. 3d, until eventually tensile loading exceeding the adhesion threshold develops normal to the contact plane of the contact joints resulting in the contact joints disappear and thus causing the two circular bodies to pull apart, as seen in Fig. 3e.

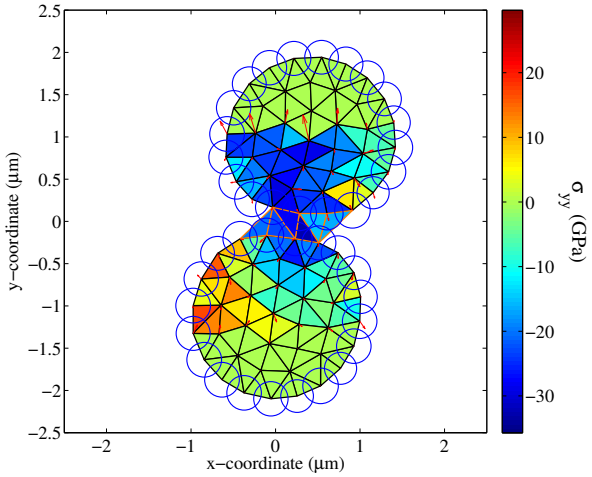

(c) Snapshot at t = 4.363 ns

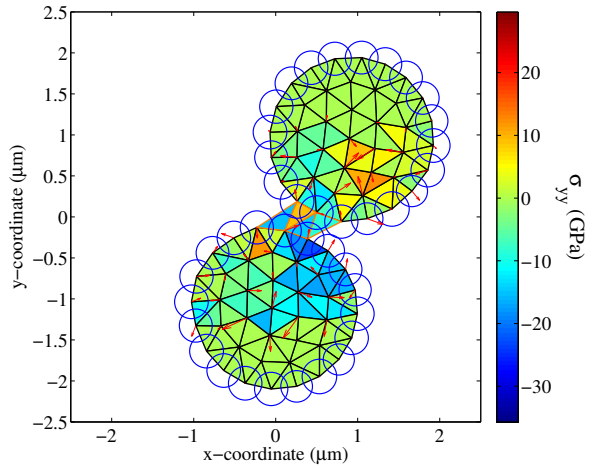

(d) Snapshot at t = 6.578 ns

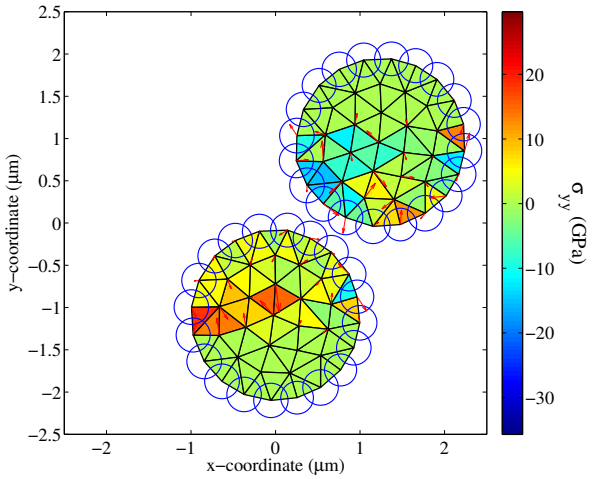

(e) Snapshot at t = 7.999 ns

Fig. 3. Snapshots of the simulation of circles in contact.

4.2. Asperity contact and break-off

In the second simulation, a moving asperity of a rough surface encounters an obstacle which causes the asperity to break off the surface. At the start of the simulation, the top body is brought down to come into contact with the circular obstacle, which is held in place during the simulation, and then it begins moving right. In Fig. 4a, the contact between the asperity and the obstacle is modeled by the orange-bordered contact joints that form between the elements within the top body and the element within the circular obstacle.

As the top body moves to the right, shown in Fig. 4, the impeding obstacle causes interior joints in the top body to progressively fracture from elastic strain until eventually the entire left asperity breaks off from the rest of the body. The fragmented asperity is then a third-body wear debris particle that is free to move within the simulation under its dynamic forces. In fact, there are five third-body particles in Fig. 4c: one is the large asperity fragment, the second is a small triangular body made from three discrete elements, and the remaining three third-body particles are each single discrete elements that are adhering to the surface of the top body.

4.3. Block sliding down inclined plane

The simulation of a block sliding down an inclined plane under the force of gravity provides a partial validation of some of the capabilities of the model. In particular, the simulation needs to accurately model the contact and friction between the block and surface on which the block is sliding. Long-distance sliding requires the remeshing capabilities of the model to maintain a smooth always present contact between the block and plane. The friction model of the contact joints needs to be capable of accurately modeling the transition from stick to slip so that the block does not start sliding until the force pulling on the block exceeds the static friction force.

In order to provide the validations desired, we first set up the geometry of a block resting on an inclined plane. A union of the geometries of the plane inclined at an angle of 15° and the block on top of it, is first used in a energy minimization simulation to find the static equilibrium state of the body under the force of gravity ($g = 98\,\mathrm{nm\,ns^{-2}}$). The minimization of the potential energy is done through steepest descent using the gradient of the energy (the forces on the elements) until the criteria on the forces is satisfied such that the system reaches a state close to static equilibrium (at least enough to reduce severe bounces in the later dynamic simulation).

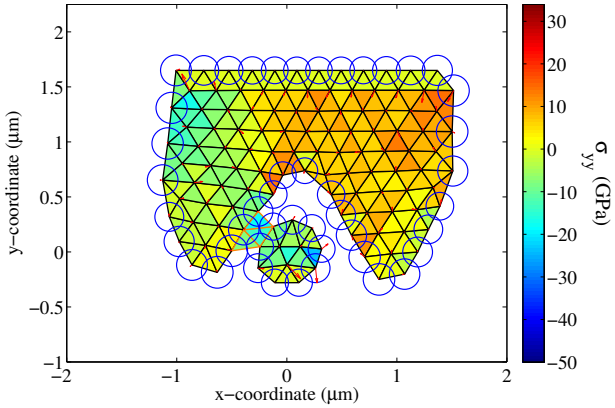

(a) Snapshot at $t = 4.098$ ns

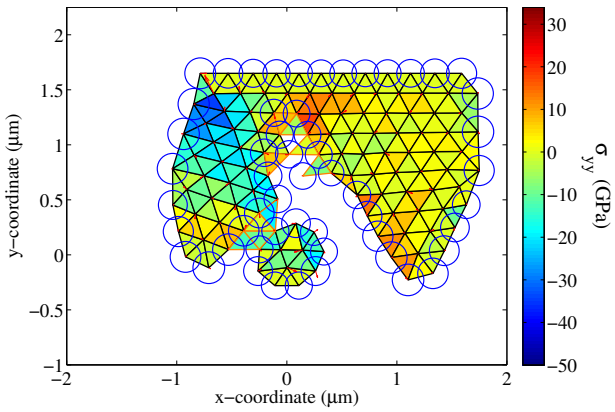

(b) Snapshot at $t = 5.356$ ns

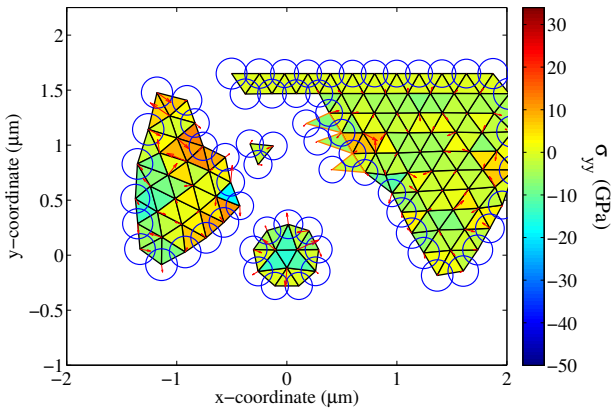

(c) Snapshot at $t = 6.988$ ns

Fig. 4. Snapshots of the simulation of asperity contact and break-off.

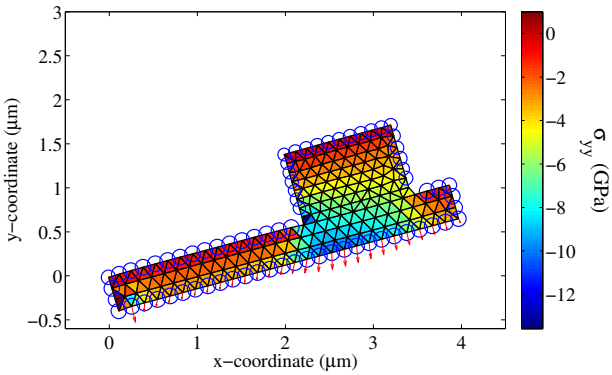

Fig. 5. State of block and inclined plane geometries under gravity after relaxing with energy minimization.

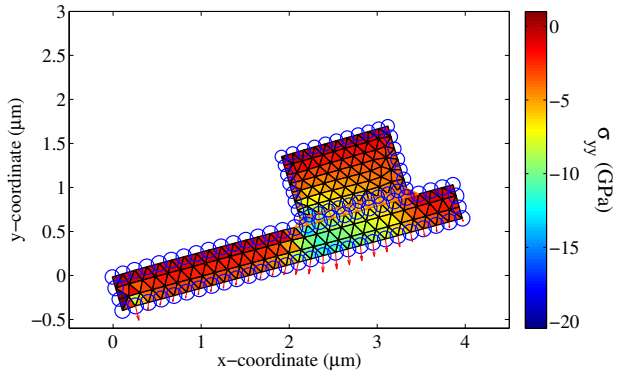

Fig. 6. Block on inclined plane under a state of stick.

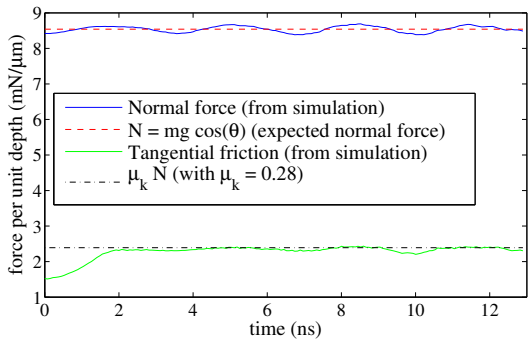

Fig. 7. Forces acting on the contact surface of the non-sliding block on an inclined plane.

Fig. 5 shows the state of the system after the minimization procedure. The interior joints in the interface between the block and the plane are then converted into contact joints with the same reference configuration to keep the same state of stress, which separates the block and the inclined plane into two different bodies ready for the dynamic simulation.

Simulations are run in order to identify two regimes of sliding: stick and slip. The block is expected to slide when the static coefficient of friction is less than tangent of the angle of the incline. Instead of altering the angle of the inclined plane, which would require a re-minimization procedure, the coefficients of friction are modified for various dynamic simulations. Through these simulations we were able to identify that the transition between stick to slip occurred when the static coefficient of friction $\mu_s < \tan(15°) \approx 0.268$, as expected. The details of two particular simulations, one for stick and one for slip, are included below.

The dynamic simulation of the block on an inclined plane with a static and kinetic coefficient of friction of $\mu_s = \mu_k = 0.28$ is used to demonstrate sticking. At the start of the simulation, there is a very slight downward movement in which a new leading contact joint is created, but then the block stops moving and remains fixed for the rest of the simulation, see Fig. 6. The tangential and normal forces on the contact surface of the block, seen in Fig. 7, show how the forces match what is expected from a simple free-body diagram analysis of a rigid block on an inclined plane. The tangential force of friction actually increases from a lower value to the expected result during the beginning of the simulation which coincides with the initial downward movement noticed in the dynamic simulation. The normal force slightly oscillates around the expected normal force, most likely due to the initial configuration not being perfectly in the static equilibrium state.

Another dynamic simulation, this time with a static coefficient of friction $\mu_s = 0.25 < \tan(15°)$ and a kinetic coefficient of friction $\mu_k = 0.20$, is used to demonstrate the case of the block sliding down the inclined plane. The block immediately begins sliding down at the start of the simulation. A snapshot of the simulation as the block is sliding down the plane can be seen in Fig. 8. The tangential and normal forces on the contact surface of the sliding block are similar to that of the non-sliding block, in that they both slightly oscillate around the forces expected from a free-body diagram analysis. One important difference, however, is that the friction force on the sliding block is $\mu_k N$ as expected, not $\mu_s N$, where N is the normal force. By calculating the time derivative of the position of the center of mass of the block, the speed at which the block was sliding down

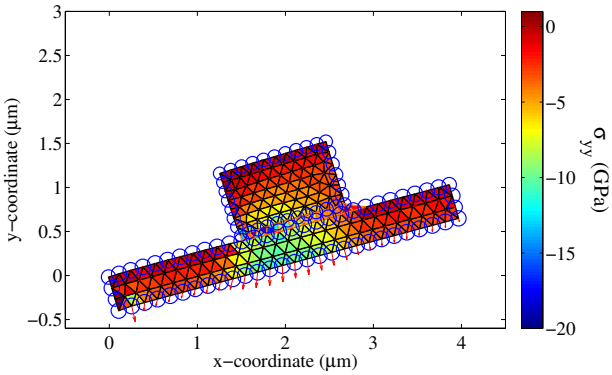

Fig. 8. Block sliding down an inclined plane under gravity.

the inclined plane was plotted versus time. The plot was very close to linear, and fitting a line to the data gave a slope of approximately 6.1 nm ns^{-2} for the line, which is the acceleration of the sliding block. From a free-body analysis of a rigid block on the inclined path, the net acceleration of the block is given by $g(\sin(\theta)-\mu_k\cos(\theta)) \approx 6.4\,\mathrm{nm\,ns^{-2}}$, which is less than a 5% difference from the measured acceleration from the simulation results.

5. Discussion

As discussed in the introduction, finite element simulations of fretting have been coupled with Archard's law or other work-rate type models to estimate the wear rates over the contact interfaces. Some of these approaches have also adjusted the geometry of the wearing surfaces according to the estimated wear rates by changing finite element node positions and using adaptive remeshing. While these approaches work fine, they do not consider the presence of discrete third body wear debris at the contact interface. Adding in additional bodies meshed using finite elements to interact through contact in the wear process presents challenges and enormous complexity for the typical contact algorithms used in the finite element method (FEM). All surfaces that may possibly come into contact need to be defined prior to starting or continuing FEM simulations. However, in a wear problem, new surfaces will be generated due to wear as the simulation progresses. So, it is not known *a priori* which finite elements will be participating in contact with other finite elements.

The model presented in this paper is able to dynamically update the set of entities that can be in contact over time. Contact is handled using the dynamically created and destroyed contact joints between discrete elements. There is no master/slave contact algorithm between triangular (in 2-D) geometries which need to be marked as capable of contact with other triangular geometries as would be the case in FEM; instead all surface elements have the potential to join together into a contact joint with nearby neighboring surface elements. This flexibility allows the model to handle contact between the two fretting surfaces, between third bodies and the fretting surfaces, and between any number of third bodies, regardless of whether the third body or fretting surface existed in its current form at the start of the simulation or if it was generated over time through the wear process.

This sort of flexibility in contact is also present in the discrete element method (DEM). An easy, scalable contact algorithm is important in the types of problems typically used in DEM simulations, such as the flow of granular materials. However, there are considerable limitations with DEM that make it unsuitable for fretting wear simulations. The most important is the fact that the particles modeled by DEM are rigid. Without the ability to model stress state in say a third-body modeled using the discrete elements of DEM, there is no accurate way of modeling the fracture of the wear debris particle into multiple smaller particles. This capability is immensely useful in simulating problems like comminution, but its also very important in fretting wear. Furthermore, if the fretting surfaces were also modeled using rigid DEM elements then fracture of asperities would also not be possible. The other major issue with the capabilities of DEM is that its contact model is too simple. Contact in DEM between the rigid particles is typically modeled using a penalty method or Hertz contact and may even include enhancements such as adhesion, see [12]. However, there is no clear way of adding friction between contacting elements in DEM that could allow the method to accurately simulate the problem of the block sliding down an inclined plane discussed in this paper.

A hybrid approach between DEM and FEM may help resolve some these issues. In fact, the method presented in this paper might be considered to be a conceptual hybrid between DEM and FEM. However, the hybrid method typically used in the literature is the combined finite-discrete element method developed by Munjiza [27], in which the discrete particles typically modeled in DEM are discretized by a finite element mesh. While this method would allow for accurately computing the stress state in both the fretting bodies and the third bodies so that the fracture of wear debris and asperities would be possible, it still shares the same problems of

DEM in terms of having difficulty accurately modeling friction between the discrete particles. Furthermore, using traditional FEM contact algorithms in this hybrid method would remove the advantages of an easy DEM-like contact algorithm, resulting in the previously discussed problems of FEM contact modeling of a third-body layer with many dynamically-generated discrete wear debris particles.

The small simulations in this paper merely provide a demonstration of the capabilities of the model. The model is flexible enough to allow asperities on the rough surface of a fretting body to fracture and become third-body wear debris which can continue to interact through contact and friction with all of the other bodies in the simulation. Also, the problem of the block sliding down the inclined plane shows how the same contact and friction algorithm in the model is capable of simulating the block sliding down the plane that is consistent with results expected from a simple free-body diagram analysis of a rigid sliding block with a Coulomb friction model. The acceleration from the simulation is within 5% of the acceleration calculated from the analytical result derived from the simplified free-body diagram analysis. In particular, the acceleration from the simulation results are less than analytically calculated acceleration, which is expected because there are slight vibrations during sliding and that vibrational energy is transferred into the bulk of elastic block, whereas in the free-body analysis the block is rigid and the sliding is considered to be perfectly smooth.

While the results from sliding block problem are consistent, further friction validation studies are needed to better validate the friction and contact capabilities of this model. The study of Hertz contact between an elastic circular body and a flat with an oscillating sliding motion can be another great validation study because analytical expressions are known for parameters like the size of the stick and slip region, the pressure and shear distribution over the contact surface, and the frictional work done per fretting cycle [28].

The other capabilities of the model, such as fracture, need validation as well. A simulation of comminution, in which brittle materials are successively crushed and grinded together, can provide some validation for the fracture and contact capabilities of this model. Results from the simulation such as the size, shape, and number of particles from the process can be compared with results from comminution experiments.

Finally, the purpose of this model is to apply it to fretting wear simulations to better understand the fretting mechanisms and how they change with different operating conditions. So, even in 2-D, simulations of fretting wear between two rough surfaces, similar in concept to the asperity fracture simulations presented in this paper but at much larger size, can be conducted to study the mechanisms of fretting wear of brittle materials. Parameters that can be varied in the set of simulations include normal load, slip amplitude, surface roughness, presence of an initial third-body wear debris layer of different compositions (number of particles, and size/shape of particles), oscillation frequency, and variants in the fretting motion such as a combined sliding and impact motion. Through qualitative analysis of the wear process and quantitative measurements of the amount of wear in the simulations, an understanding of the dependence of fretting wear behavior on the operating conditions can be obtained and a fretting wear mechanism map can be created.

6. Conclusion

A model for simulating fretting wear of brittle materials at the micron length-scale is proposed which has the capabilities of generating wear debris and handling contact between the any bodies present in the dynamic simulation, including new bodies generated during the evolution of the simulation due to fracture of asperities. Experimental results have shown work-rate wear models with constant wear coefficients are insufficient for modeling fretting wear under the variety of operating conditions that may occur. The model proposed in this paper can be used to better understand how the wear coefficient changes with some relevant operating conditions by studying how changes in the operating conditions affect the mechanisms of wear in the simulations. Results and analysis from future simulations using this model can provide tools, such as a wear mechanism map, to improve wear rate estimates in fretting wear problems like the case of grid-to-rod fretting in nuclear fission reactors.

Acknowledgements

We acknowledge Professors Ken Kamrin and David Parks at the Massachusetts Institute of Technology for helpful discussions and guidance. Also we gratefully acknowledge the Consortium for Advanced Simulation of Light Water Reactors (CASL), a US Department of Energy innovation hub, for sponsorship of this effort.

References

[1] K.-T. Kim, The study on grid-to-rod fretting wear models for PWR fuel, Nuclear Engineering and Design 239 (2009) 2820–2824.

[2] P. R. Rubiolo, Probabilistic prediction of fretting-wear damage of nuclear fuel rods, Nuclear Engineering and Design 236 (2006) 1628–1640.
[3] P. R. Rubiolo, M. Y. Young, On the factors affecting the fretting-wear risk of PWR fuel assemblies, Nuclear Engineering and Design 239 (2009) 68–79.
[4] J. F. Archard, Contact and rubbing of flat surfaces, Journal of Applied Physics 24 (1953) 981–988.
[5] S. Fouvry, P. Kapsa, H. Zahouani, L. Vincent, Wear analysis in fretting of hard coatings through a dissipated energy concept, Wear 203 (1997) 393–403.
[6] I. Goryacheva, P. Rajeev, T. Farris, Wear in partial slip contact, Journal of Tribology 123 (2001) 848–856.
[7] A. T. Kasarekar, N. W. Bolander, F. Sadeghi, S. Tseregounis, Modeling of fretting wear evolution in rough circular contacts in partial slip, International Journal of Mechanical Sciences 49 (2007) 690–703.
[8] I. McColl, J. Ding, S. Leen, Finite element simulation and experimental validation of fretting wear, Wear 256 (2004) 1114–1127.
[9] C. Paulin, S. Fouvry, C. Meunier, Finite element modelling of fretting wear surface evolution: Application to a Ti-6A1-4V contact, Wear 264 (2008) 26–36.
[10] J. F. Molinari, M. Ortiz, R. Radovitzky, E. A. Repetto, Finite-element modeling of dry sliding wear in metals, Engineering Computations 18 (2001) 592–610.
[11] J. Ding, I. McColl, S. Leen, P. Shipway, A finite element based approach to simulating the effects of debris on fretting wear, Wear 263 (2007) 481–491.
[12] I. Iordanoff, B. Seve, Y. Berthier, Solid third body analysis using a discrete approach: influence of adhesion and particle size on macroscopic properties, Journal of Tribology 124 (2002) 530–538.
[13] M. P. Szolwinski, T. N. Farris, Mechanics of fretting fatigue crack formation, Wear 198 (1996) 93–107.
[14] A. E. Giannakopoulos, S. Suresh, A three-dimensional analysis of fretting fatigue, Acta Materialia 46 (1998) 177–192.
[15] H. Attia, A generalized fretting wear theory, Tribology International 42 (2009) 1380–1388.
[16] T.-H. Kim, S.-S. Kim, Fretting wear mechanisms of Zircaloy-4 and Inconel 600 contact in air, KSME International Journal 15 (2001) 1274–1280.
[17] K. H. Cho, T. H. Kim, S. S. Kim, Fretting wear characteristics of Zircaloy-4 tube, Wear 219 (1998) 3–7.
[18] N. P. Suh, The delamination theory of wear, Wear 25 (1973) 111–124.
[19] H.-K. Kim, S.-J. Kim, K.-H. Yoon, H.-S. Kang, K.-N. Song, Fretting wear of laterally supported tube, Wear 250 (2001) 535–543.
[20] H.-K. Kim, Y.-H. Lee, Influence of contact shape and supporting condition on tube fretting wear, Wear 255 (2003) 1183–1197.
[21] H.-K. Kim, Y.-H. Lee, K.-H. Lee, On the geometry of the fuel rod supports concerning a fretting wear failure, Nuclear Engineering and Design 238 (2008) 3321–3330.
[22] Y.-H. Lee, H.-K. Kim, Effect of spring shapes on the variation of loading conditions and the wear behaviour of the nuclear fuel rod during fretting wear tests, Wear 263 (2007) 451–457.
[23] H.-K. Kim, Y.-H. Lee, Wear depth model for thin tubes with supports, Wear 263 (2007) 532–541.
[24] Y.-H. Lee, H.-K. Kim, Y.-H. Jung, Effect of impact frequency on the wear behavior of spring-supported tubes in room and high temperature distilled water, Wear 259 (2005) 329–336.
[25] A. Iwabuchi, The role of oxide particles in the fretting wear of mild steel, Wear 151 (1991) 301–311.
[26] Y. Basar, D. Weichert, Nonlinear Continuum Mechanics of Solids: Fundamental mathematical and physical concepts, Springer, 2000.
[27] A. Munjiza, The Combined Finite-Discrete Element Method, Wiley, 2004.
[28] R. D. Mindlin, Compliance of elastic bodies in contact, ASME Journal of Applied Mechanics 16 (1949) 259–268.